

Harnessing Optoelectronic Noises in a Photonic Generative Adversarial Network (GAN)

Changming Wu¹, Xiaoxuan Yang², Heshan Yu³, Ruoming Peng¹, Ichiro Takeuchi³, Yiran Chen²

and Mo Li^{1,4,*}

¹*Department of Electrical and Computer Engineering, University of Washington, Seattle, WA 98195, USA*

²*Department of Electrical and Computer Engineering, Duke University, Durham, NC 27708, USA*

³*Department of Materials Science and Engineering, University of Maryland, College Park, MD 20742, USA*

⁴*Department of Physics, University of Washington, Seattle, WA 98195, USA*

ABSTRACT

Integrated programmable optoelectronics is emerging as a promising platform of neural network accelerator, which affords efficient in-memory computing and high bandwidth interconnectivity. The analog nature of optical computing and the inherent optoelectronic noises, however, make the systems error-prone in practical implementations such as classification by discriminative neural networks. It is thus imperative to devise strategies to mitigate and, if possible, harness optical and electrical noises in photonic computing systems. Here, we demonstrate a prototypical photonic generative adversarial network (GAN) that generates handwritten numbers using a photonic core consisting of an array of programmable phase-change optical memory cells. We harness optoelectronic noises in the photonic GAN by realizing an optical random number generator derived from the amplified spontaneous emission noise, applying noise-aware training by injecting additional noise to the network, and implementing the trained network with resilience to hardware non-idealities. Surprisingly, the photonic GAN with hardware noises and inaccuracies can generate images of even higher quality than the noiseless software baseline. Our results suggest the resilience and potential of more complex photonic generative networks based on large-scale, non-ideal photonic hardware. The demonstrated GAN architecture and the proposed noise-aware

* Corresponding author: moli96@uw.edu

training approach are generic and thus applicable to various types of optoelectronic neuromorphic computing hardware.

Introduction

The current rate of improvement in digital electronics' energy efficiency¹⁻³ is lagging behind the fast-growing computational load^{4,5} spurred by the widespread implementation of large-scale artificial neural networks for machine learning and artificial intelligence⁶⁻¹¹. Because of its significant advantages in power efficiency, communication bandwidth and parallelism¹²⁻¹⁹, analog optical computing based on integrated optoelectronic processors²⁰⁻²⁵ is once again brought into focus as hardware accelerators for neural networks. Photonic neural networks reported to date^{17,20,22,23,26,27} are predominantly hybrid optoelectronic networks in which the photonic components are mainly used for linear multiplication and interconnect while nonlinear functions and feedback control are still implemented electronically. Compared to electronic neural networks using digital processors, photonic neural networks have higher inaccuracy and error rates due to the analog nature of optical computing and the abundance of optoelectronic noises. The accumulation of computational errors in large-scale photonic neural networks could severely impair their performance²⁸⁻³⁰, limiting the computation effectiveness and scalability. Although several offline noise-aware training schemes have been proposed by injecting noises to layer inputs^{29,31}, synaptic weights^{28,32}, and pre-activations^{33,34} to mitigate analog hardware non-idealities such as inter-device variations^{35,36}, global temporal device performance drifts³⁰, and read/write errors²¹, they only address discriminative models. Particularly, for a discriminative network based on diffractive optics, training with carefully drafted parametric randomness can make the network robust against sole optical non-idealities such as misalignments³⁷, rescales, shift, and rotation³⁸, but the optoelectronic noises have not been considered. In contrast to discriminative models, generative neural network models can automatically discover and learn regularities or patterns from the training data to generate plausible new instances³⁹⁻⁴¹. They are having a fast-growing range of applications. So far, a photonic generative network has not been reported, and the corresponding noise-aware training strategies aiming to mitigate optoelectronic noises in such networks have not been explored.

Here, we demonstrate a photonic generative adversarial network (GAN) based on a photonic computing core consisting of a programmable optical memory based on an array of phase-change metasurface mode converters (PMMC)⁴². We train the photonic GAN to generate handwritten numbers. Unlike photonic discriminative networks which suffer from noises and errors, in the photonic GAN, we harness and mitigate optoelectronic noises and errors in three ways. First, we utilize the amplified spontaneous emission (ASE) noise to realize an optical true random number generator^{43,44} (RNG), which is used as the input to the GAN. This optical RNG efficiently generates random numbers at high speed in multiple parallel wavelength channels by spectrally slicing the ASE spectrums⁴⁴⁻⁴⁶, enabling parallelized photonic generative models. Second, we analyze error sources originating from the photonic components in the photonic GAN and propose noise-aware training approaches by augmenting noises during the training process, which improves the GAN performance and robustness. Third, we validate the training approaches through experiment and simulation, and demonstrate that the photonic GAN can benefit from the inevitable random errors in practical implementation. Surprisingly, the images generated from non-ideal photonic hardware show even higher quality than those generated by an ideal, errorless counterpart (*i.e.*, software baseline). Our results demonstrate the feasibility and resilience of more complex photonic GANs using non-ideal optoelectronic hardware. Since the proposed noise-aware training approaches are generic, they can be applied to various types of optoelectronic neuromorphic computing hardware.

Results

Photonic GAN architecture

A GAN network consists of two sub-neural network models (Fig. 1a), a generator and a discriminator⁴⁷⁻⁴⁹. These two models compete against each other in a zero-sum game: the discriminator strives to distinguish the instances produced by the generator (labeled as the “fake” instances) from the real instances in the training dataset (labeled as the “real” instances); the generator aims to fool the discriminator by producing novel instances that imitate the real instances. The competition drives both networks to improve their capabilities until an equilibrium state is reached, *i.e.*, when the “fake” instances are indistinguishable from the “real” instances by the discriminator, so the generator is deemed well-trained to generate plausible new instances. In

this work, we design a prototype photonic GAN to generate images of the handwritten number “7” based on a noise-aware offline training configuration: we first train the GAN on a computer⁵⁰ and implement the trained network model on the photonic platform (Fig. 1b). Here, we only focus on realizing the photonic generator since the photonic discriminator itself is a neural network that performs classification tasks and has been demonstrated previously by many groups, including us^{16,17,20,42}. The kernel matrices stored in the tensor core are mapped onto the PMMCs through electro-optical modulated optical pulses. As shown in Fig. 1c, in each layer of the generator, the input data is encoded in the power of the optical signals through multiple wavelength channels, processed by the PMMC photonic tensor core (Fig. 1d), and the results are detected by the photodetector arrays. Electronic post-processing is then performed to apply nonlinear functions. The results are re-encoded using electro-optic modulators into the optical signals, which are relayed to the next photonic layer. In such hardware implementation of the network, various noises, including optical and electrical noises of the optical sources, modulators and photodetectors, are accumulating through the processes of programming (*i.e.*, writing) the kernel matrices, data encoding, and data transferring (*i.e.*, reading) between the layers of the network.

Optical random number generator (RNG)

One key component of the photonic generator is the optical RNG that produces the random input. To realize it, we utilize the ASE noise from the erbium-doped fiber amplifiers (EDFA), the ubiquitous noise source in fiber-optic communication systems, to generate random optical signals at high rates in four parallel channels, as shown schematically in Fig. 2a. Here, the ASE noise from the EDFA is first filtered with wavelength division multiplexing (WDM) demultiplexers (DEMUX) and then detected with photodetectors. The generated baseband electrical currents due to beating between different frequency components are referred to as “ASE-ASE beat noises”^{51,52}. The DC photocurrent is filtered by a DC block, passing only the stochastic photocurrent variances to a sampling oscilloscope to generate random numbers (see Supplementary Information for the theory of the optical RNG). Fig. 2b and 2c plot the statistical histogram and a representative trace of the random numbers (in voltage) generated in a single WDM channel, respectively. The probability density function is well-approximated by a zero-mean Gaussian distribution with a standard deviation (STD) of 0.2 V (*i.e.*, $N(0, 0.2)$). We further calculate the correlation coefficient

of an $N=5\times 10^4$ -number long sequence (Fig. 2d), which reaches the limit of $1/\sqrt{N}$ (red line in Fig. 2d), proving the randomness of the number sequence. Because of the limited size of the photonic tensor core, we measure and record the random numbers from the RNG and repeatedly input them to the generator during the experiment. In future full-scale systems, the filtered ASE noise can be directly used as random input to the GAN.

Photonic tensor core error analysis

The other key component of the photonic generator is the photonic tensor core, which optically performs matrix-vector multiplication (MVM). The inset in Fig. 1c shows the schematic of one PMMC kernel element of the core that computes multiply-accumulate (MAC): $x \rightarrow x \cdot w + b$, the fundamental operation of MVM. The PMMC consists of an array of $\text{Ge}_2\text{Sb}_2\text{Te}_5$ (GST) nano-antennas with tapering widths (see Fig. 1e for the SEM images), forming a phase-gradient meta-surface patterned on a silicon nitride waveguide⁴². The input vector element x is encoded in the power of the input optical signal. The corresponding kernel element weight w is represented using the TE₀/TE₁ mode contrast $\Gamma = \beta_{\text{TE}0} - \beta_{\text{TE}1}$ at multiple intermediate levels between [-1..1], where the $\beta_{\text{TE}0(\text{TE}1)} = P_{\text{TE}0(\text{TE}1)} / (P_{\text{TE}0} + P_{\text{TE}1})$ is the mode purity, and $P_{\text{TE}0}$ ($P_{\text{TE}1}$) is the power of the TE₀ (TE₁) mode component in the waveguide. Thus, the MAC computation is simplified to an incoherent optical transmission measurement and can be performed over a broad bandwidth. Fig. 2e shows the evolution of Γ during the programming process of using optical control pulses to set negative (-0.7), zero (0.0), and positive (0.7) values, respectively. We implement the network model on a 2×2 tensor core with four PMMCs (Fig. 1d). The kernel weight W_{ij}^l value is mapped to the corresponding mode contrast Γ_{ij}^l as $\Gamma_{ij}^l = W_{ij}^l \cdot \left(\left| \Gamma \right|_{\max}^l / \left| W \right|_{\max}^l \right)$, where $\left| \Gamma \right|_{\max}^l$ is the maximum absolute mode contrast, $\left| W \right|_{\max}^l$ is the maximum absolute kernel weight of layer l . Given the limited number of PMMCs on a chip, we repeatedly reset the kernel elements on the same devices, which bottlenecks the computing speed. With a sufficiently large tensor core in a photonic crossbar array architecture⁵³⁻⁵⁵, one could directly map the full kernel matrices to the hardware so the computing speed will be much accelerated.

The analog nature of weight programming and data encoding and transferring in the photonic neural network limits the precisions of MVM calculations and makes the computation error-prone. The computation errors would accumulate through the layers of the network and impair the final results. Because in realistic experiments, the computation errors stem from various optoelectronic noises in the system, we use the terms of noise and error interchangeably. To quantify the noises and errors in our system, we repeatedly program different fixed Γ values and estimate the short-term inaccuracy by measuring the variation $\Delta\Gamma$. Fig. 2f shows that the STD of 15 programming operations is less than 0.7%, which is one order-of-magnitude larger than the input encoding error (see Supplementary Material for more detailed error analysis). Thus, the short-term programming inaccuracy $\Delta\Gamma$ (write error), limited by the inaccuracy of the electro-optical modulated optical pulse, is one of the dominant error sources. Another error source is the long-term measurement fluctuations (read error), including the noise of photodetectors, the variation of the O/E and E/O conversions, and the thermal fluctuation of the PCM by light absorption. These errors collectively contribute to an effective error $\Delta W_{ij}^l = \left(\left| \Gamma \right|_{\max}^l / \left| W \right|_{\max}^l \right) \cdot \Delta \Gamma_{ij}^l$ on the kernel element weight W_{ij}^l , where $\Delta \Gamma_{ij}^l$ is the total write error. To estimate the computation error of the overall system, Fig. 2g compares the measured MVM error distributions with the simulation, which assumes a Gaussian distribution. The result estimates the overall error $\Delta \Gamma_{ij}^l$ to be 5%, which we subsequently use in the noise-aware training and simulation.

Unlike the discriminative network where the input regularities or patterns are well-defined, the GAN takes random numbers as the input and would be more susceptible to the effective weight setting noise ΔW_{ij}^l , which could degrade the quality of the generated new instances^{56,57}. To reveal the noise effect on the GAN, we emulate the noisy hardware on a GAN model that is trained using a noiseless offline training approach but add a random error ΔW_{ij}^l (introduced by $\Delta \Gamma_{ij}^l$ with a Gaussian distribution $N(0, 0.05)$) when using it to generate images. Fig. 3a plots 49 images of 14×14 pixels generated from simulation using random inputs produced by the optical RNG. These images show the handwritten “7” but have very noisy backgrounds, demonstrating that the original training algorithm is impaired by the practical weight setting noise (see Supplementary Information for the detailed comparison between the GAN inference using accurate kernel and inaccurate kernel).

Therefore, it is necessary to take hardware noise into consideration during training to realize a GAN that is resilient to realistic noises. Theoretically, it has been proven that adding noises to the training data of a neural network is equivalent to an extra regularization added to the error function³¹, which can significantly improve hardware noise tolerance in a discriminative neural network. Meanwhile, it was shown that introducing noise on kernel weights during training enhances the robustness against weight perturbations of multi-layer perceptrons²⁸, and inference accuracy close to the software baseline could be achieved. However, previous demonstrations of noise-aware solutions are limited to discriminative networks. For GAN, theoretical, simulation, and experimental validations of effective noise-aware solutions still lack and require further investigation.

Noise-aware training of photonic generative model

For our photonic GAN, we propose and experimentally validate two noise-aware training approaches, namely, the input-compensatory approach (IC-GAN) and the kernel weight-compensatory approach (WC-GAN), to improve the tolerance of the network to the effective weight setting noise ΔW_{ij}^l . The IC-GAN approach inflates the STD of the random signal input from 0.2 V, the experimental value, to 0.5 V during training. The WC-GAN approach adds $\Delta \Gamma_{ij}^l$ with 5% STD to the corresponding weight at each forward-propagation pass but performs noiseless gradient descent in the back-propagation pass (see Fig. 1b and Supplementary Information for the training procedure for these noise-aware training approaches). Fig. 3b and Fig. 3c show the experimentally generated images of handwritten “7” by the photonic GAN trained using both noise-aware approaches. For a fair comparison, the random number inputs used for inferences are produced by the same optical RNG. Compared to the images generated by the original GAN (Fig. 3a), the images generated using both noise-aware approaches display much clearer handwritten “7” patterns with lower background noise, thus validating the noise tolerance of the IC-GAN and WC-GAN. Furthermore, we observe the images generated by the WC-GAN (Fig. 3c) have richer handwritten-like features than those by the IC-GAN (Fig. 3b), with more diverse variations in handwritten-like styles. Therefore, we conclude that the WC-GAN is more advantageous for practical implementation using non-ideal analog hardware.

Discussion

To quantitatively compare the GAN performance, we use the standard metric of Frechet inception distance (FID), which evaluates both the fidelity and diversity of the generated images by comparing the feature distribution in the generated images with images from the training dataset. The lower the FID score, the better performance of the GAN⁴⁹. In Fig. 3d, the FIDs of the images generated by the original-GAN^{35,49,58}, the IC-GAN, and the WC-GAN, respectively, are compared, assuming either ideal ($\text{FID}_{\text{ideal}}$) or noisy ($\text{FID}_{\text{noisy}}$) hardware (see Supplementary Information for detailed steps to calculate the FID). The $\text{FID}_{\text{noisy}}$ (hashed bars in Fig. 3d) is the lowest for the WC-GAN and the highest for the original-GAN, consistent with the observation in Fig. 3a-c. The impact of hardware noise $\Delta\text{FID} = \text{FID}_{\text{noisy}} - \text{FID}_{\text{ideal}}$ is plotted in Fig. 3e. The noise-aware WC-GAN and IC-GAN clearly show two notable benefits. First, the $\text{FID}_{\text{ideal}}$ (solid bars in Fig. 3d) for the WC-GAN is lower than the original-GAN (e.g., the software baseline), indicating that introducing noises during training helps GAN learn better. Such a gain is absent in discriminative networks, where the inference accuracies of the noise-aware trained model cannot exceed the software baseline^{29,30,33,34}. Second, surprisingly, the noise impact results (Fig. 3e) show that, unlike the original-GAN, the WC-GAN and IC-GAN implemented on the photonic hardware with practical noise (hashed bars in Fig. 3d) perform even better in inference than the noiseless hardware (solid bars in Fig. 3d). In contrast, a discriminative network's inference accuracy always decreases with more noisy hardware^{37,38}. This surprising gain in performance suggests photonic neural networks' potential in generative models despite the inevitable optoelectronic noises and errors.

To predict if the noise-aware approaches performance gain is scalable, in simulation, we train a larger-scaled GAN to generate images of all 10 number digits, using ideal or noise-aware approaches under various levels of writing errors. Fig. 4a shows the FID score of the results as a function of $\Delta\Gamma_{ij}^l$. Here, the curvature regularization approach (CR-GAN), which evolves from the WC-GAN, is used to improve the GAN robustness further (see the Supplementary Information for more details about the CR-GAN). The comparison shows that the CR-GAN performs better than the original GAN at every error level. Note that under our present realistic noise level of 5% (Fig. 3g), the FID of CR-GAN is still below the software baseline, whereas the original GAN's FID is higher than the baseline. For both approaches, with the increasing noise level, the FID first drops until reaching a local minimum at ~2.5% noise and then increases. To explain this, we further examine the images generated by CR-GAN at three noise levels: 0%, 5%, and 10% in Fig. 4b-d.

The comparison shows that the increasing hardware noise in GAN would improve the diversity (evaluated by the STD of the percentage of each number classes in the generated images⁵⁶, see Supplementary Information for more details) but at the same time reduce the fidelity of the generated images⁵⁶. The trade-off results in a minimal FID at ~2.5% noise as in Fig. 4a. Throughout the full range of noise levels, the noise-aware approach consistently improves the GAN over the noiseless approach.

In conclusion, we demonstrate a photonic GAN network based on phase-change photonics by utilizing the intrinsic noise sources in the photonic system. Unlike the previously demonstrated discriminative networks that suffer from the hardware noise, our experimental and simulation results show the photonic GAN can not only tolerate but also benefit from a certain level of hardware noise when using noise-aware training approaches. Our finding expands the current implementation of photonic neural networks to generative models⁵⁹, in which the inevitable and ubiquitous optoelectronic noises and errors can be mitigated and even leveraged in intelligent ways. We emphasize that the proposed noise-aware training approaches are generic and thus applicable to various types of optoelectronic neuromorphic computing hardware, the improved resilience of the proposed model designs to the noises also implies their scalability in large-scale photonic neural networks with tightly co-integrated electronics and photonics.

Materials and Methods

PMMC design and fabrication

The PMMC is made of a phase-gradient GST antennas array. The scattered phase difference and the spatial distance between adjacent antennas are design to assist convert the incident TE₀ mode into the TE₁ mode when GST is in the crystalline phase while maintaining the TE₀ mode when GST is in the amorphous phase. To fabricate PMMC, a 30nm thick GST film is deposited by sputtering on a Si₃N₄ on an oxidized silicon substrate. The GST then are patterned into antennas using standard electron beam lithography (EBL) process followed by an inductively coupled plasma (ICP) etching process on Si₃N₄ photonic structures. A 218 nm thick Al₂O₃ layer is conformal coated on GST as the capping layer.

Measurement setup

The measurement set up to operate the photonic tensor core is shown in Fig. S2. To avoid interference, the input optical signals are carried by four different wavelengths using four tunable CW lasers, with their amplitude controlled by the 1 kHz variable optical attenuators (VOA). An additional controlled laser with a 1×4 optical switch is used to selectively program the pre-trained network weight into each GST PMMC using optical pulses. The controlled optical pulse is generated with a 12 GHz electro-optical modulator and power amplified by the low noise erbium-doped fiber amplifier (EDFA). The energy of each controlled pulse is further precisely controlled using another VOA. Both the input signals and the controlled pulses are coupled into the photonic device through the integrated grating couplers with a coupling efficiency of $\sim 20\%$. The input signals are fed forward through each input channel while the controlled pulses are count propagate through the TE_1 detection channels. The optical power in TE_0 mode is collected on-chip using integrated Y-junctions and detected while the optical power in TE_1 mode is collected off-chip first and combined during the post-process and the mode power contrast is then calculated which gives the MVM results.

FIGURES

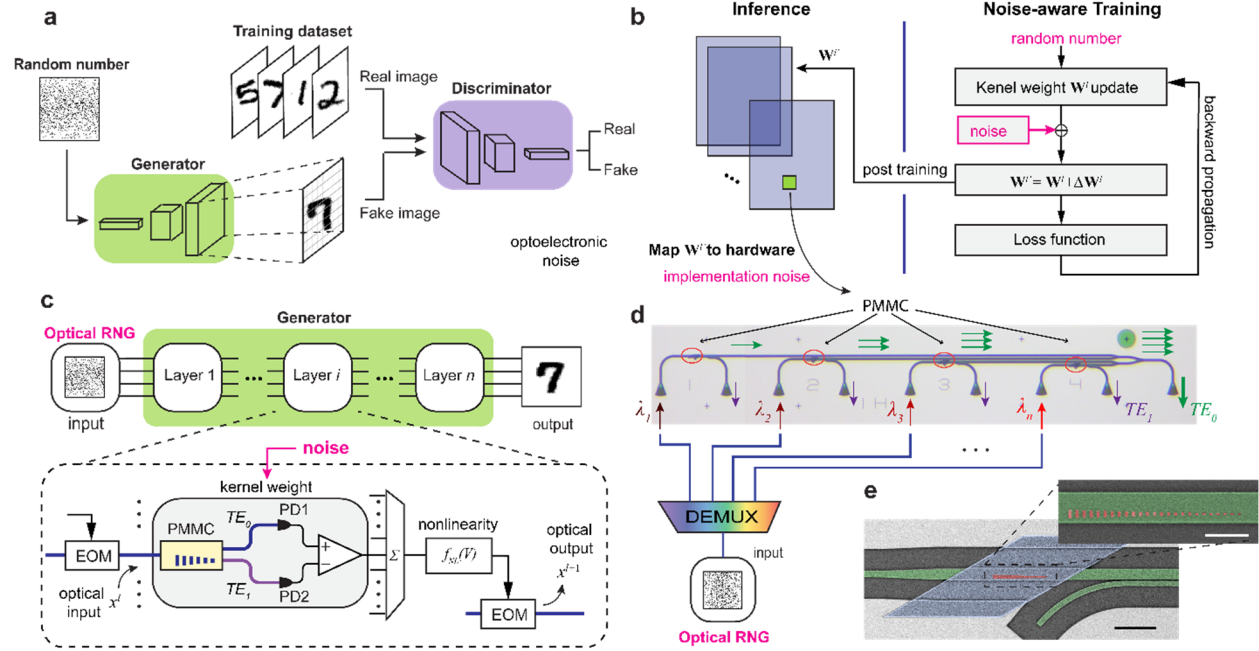


Figure 1 Photonic GAN network with optoelectronic noises. **a.** The general GAN framework is composed of two sub-network models, a generator and a discriminator. The generator competes with the discriminator during training and could generate new instances after it is trained. **b.** The offline noise-aware training and inference processes flow of the generator. The process of mapping the trained weight to the hardware during the implementation inevitably introduces the optoelectronic noise. **c.** Decomposition of the generator into individual layers. In each layer, the input signals pass through the photonic tensor core and are converted to the electrical domain by photodetectors (PDs). After post-processing, the data is converted back into the optical domain and then transfer to the next layer. **d.** Optical microscopic image of the photonic tensor core consisting of four input channels. **e.** The detailed false-colored SEM image of the photonic tensor core. The Si_3N_4 waveguide, the GST metasurface and the Al_2O_3 protection layer are colored green, red, and blue, respectively. Scale bar: 10 μm . Inset: the zoomed-in SEM image of the phase-gradient metasurface on the waveguide. Scale bar: 2 μm .

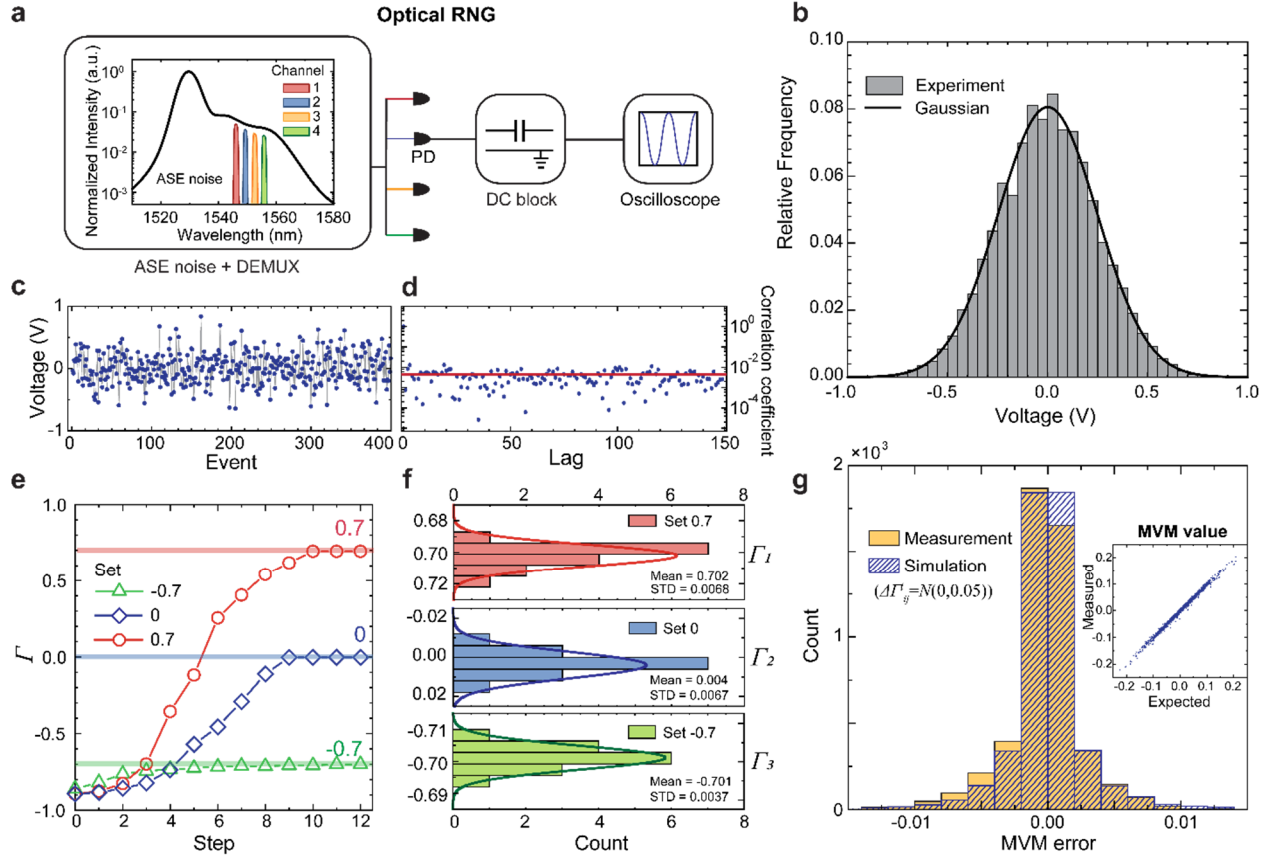


Figure 2 Optital RNG and kernel programming errors. **a.** Schematic of the optical RNG. The ASE noise is spectrally sliced into 4 wavelength channels using DEMUX and then detected with square-law photodetectors. After a DC block, the random electrical signals are sampled by an oscilloscope. **b.** and **c.** Statistical histograms (**b**) and a representative trace (**c**) of the generated random numbers. The generated random number follows the Gaussian distribution. **d.** Correlation coefficient as a function of lag for the random number sequence. A random number sequence with length $N = 5 \times 10^4$ has a correlation coefficient (blue dots) around the lower limit $1/\sqrt{N}$ (red line). **e.** Process of programming the mode contrast of a kernel element using optical pulses. The target Γ values are -0.7, 0, and 0.7, respectively. **f.** Histogram of Γ value distribution when the kernels are repeatedly set to be -0.7, 0, and 0.7, respectively. The standard deviation for each setting is 0.37%, 0.67%, 0.68%, respectively. **g.** Histograms of the error distribution obtained by experimental measurement (solid) and the simulation (hatched) when assuming the $\Delta\Gamma_{ij}$ follow a Gaussian distribution with a standard deviation equal to 5%. Inset: Measured MVM accuracy for 4900 MVM operations in the first layer of the network.

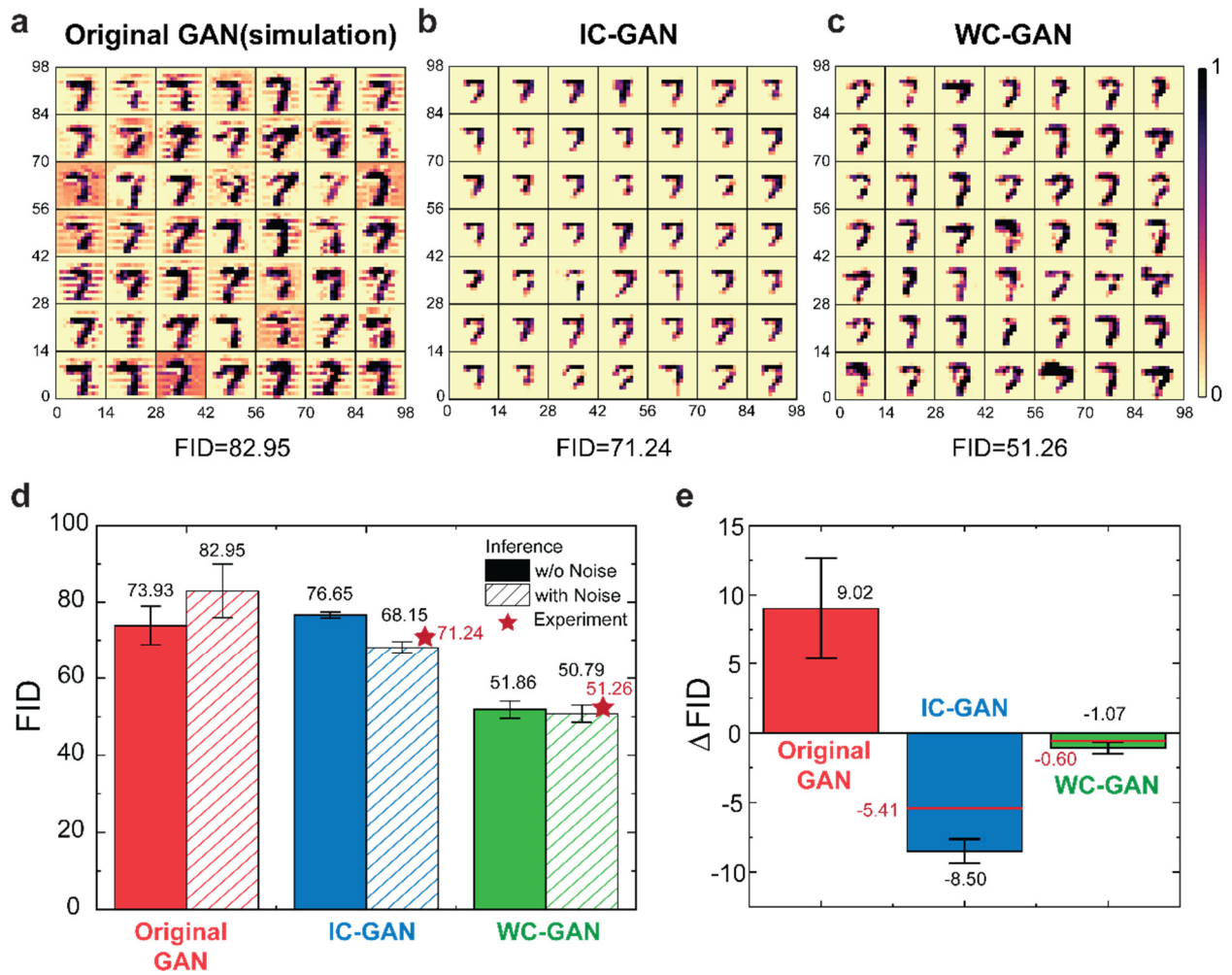


Figure 3 Generating handwritten numbers with GAN. **a-c:** 49 images (size: 14×14 pixels) generated by **(a)** original-GAN, **(b)** IC-GAN, and **(c)** WC-GAN under effective kernel weight setting error (introduced by 5% Gaussian random error $\Delta\Gamma_{ij}^l$) using random inputs $\sim N(0,0.2)$ produced by the optical RNG. **(a)** is generated by simulation, **(b)** and **(c)** are the outputs from experiments. **d.** The FIDs of the generated images assuming the network is trained using various approaches and is implemented either on the ideal (solid bars) or noisy practical hardware (hashed bars). The FIDs obtained from the experimental results are labeled as stars. **e.** The Δ FID of the images generated by the same GAN using the same random input but performing inferences using a noiseless (simulation) or practical hardware (simulation and experiment), respectively. The Δ FIDs calculated from experimentally generated images are denoted by the red lines.

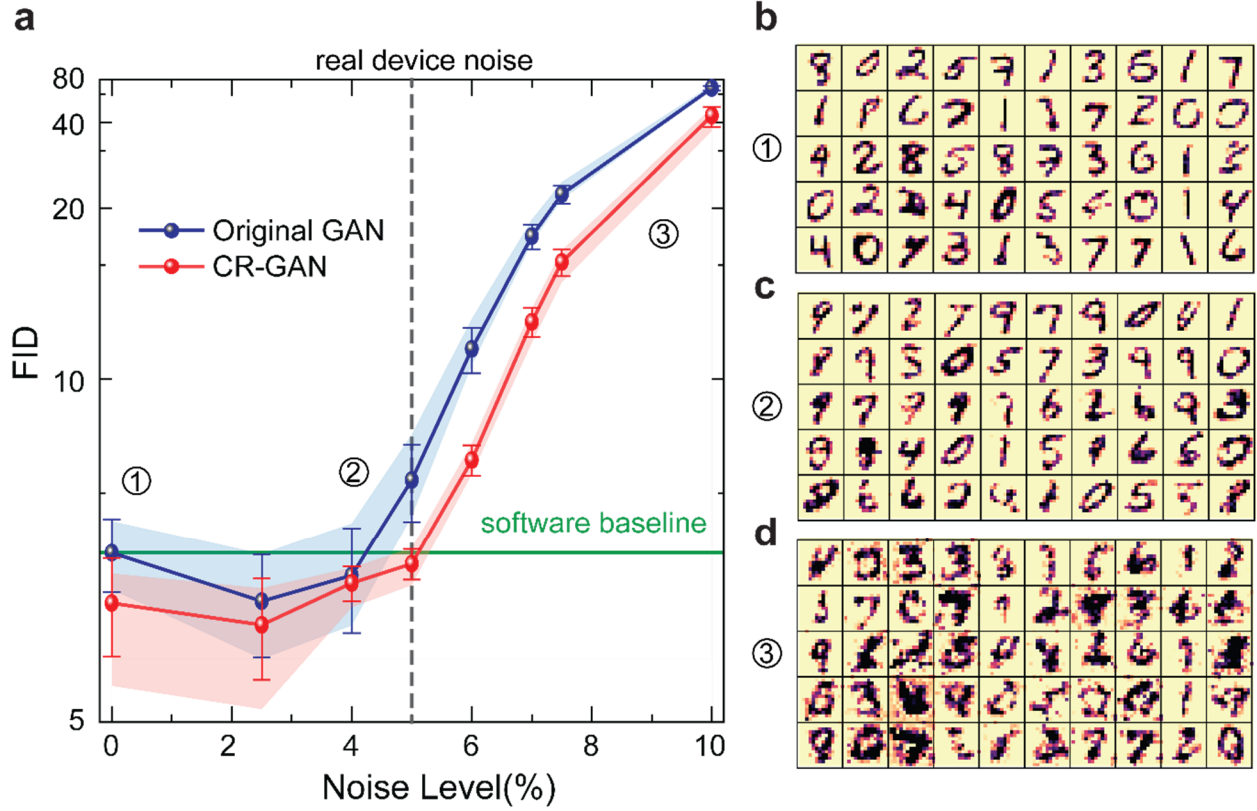


Figure 4 Scalability of noise-aware training. **a.** The FID of the generated images by original GAN and CR-GAN respectively under various effective mode contrast setting noise $\Delta\Gamma_{ij}^l$ with STD ranging from 0% to 10%. The shaded region indicates the range of FID over 5 individual tests. The FID is lower for CR-GAN at every noise level. Under 5% practice noise (black dashed line), the FID for CR-GAN is below the software baseline (solid green line) while the FID for the original GAN is above it. **b-d:** 50 images (size: 14×14) generated by curvature-regularization GAN assuming under effective mode contrast setting noise of **(b)** 0%, **(c)** 5%, **(d)** 10%.

Reference:

1. Marr, B., Degnan, B., Hasler, P. & Anderson, D. Scaling energy per operation via an asynchronous pipeline. *IEEE Transactions on Very Large Scale Integration (VLSI) Systems* **21**, 147–151 (2013).
2. M. Mitchell Waldrop. More than Moore. *Nature* **530**, 145–147 (2016).
3. Theis Thomas N & H.-S. Philip Wong. The End of Moore’s Law: A New Beginning for Information Technology. *Computing in Science & Engineering* **19**, 41–50 (2017).
4. Nicola Jones. How to stop data centres from gobbling up the world’s electricity. *Nature* **561**, 163–166 (2018).
5. Xu, X. *et al.* Scaling for edge inference of deep neural networks. *Nature Electronics* **1**, 216–222 (2018).
6. Simonyan, K. & Zisserman, A. Very Deep Convolutional Networks for Large-Scale Image Recognition. *arXiv preprint arXiv:1409.1556* (2014).
7. Mnih, V. *et al.* Human-level control through deep reinforcement learning. *Nature* **518**, 529–533 (2015).
8. Yann LeCun, Yoshua Bengio & Geoffrey Hinton. Deep learning. *Nature* **521**, 436–444 (2015).
9. Silver, D. *et al.* Mastering the game of Go with deep neural networks and tree search. *Nature* **529**, 484–489 (2016).
10. Chen, Y. H., Krishna, T., Emer, J. S. & Sze, V. Eyeriss: An Energy-Efficient Reconfigurable Accelerator for Deep Convolutional Neural Networks. *IEEE Journal of Solid-State Circuits* **52**, 127–138 (2017).
11. Yao, P. *et al.* Fully hardware-implemented memristor convolutional neural network. *Nature* **577**, 641–646 (2020).
12. Brunner, D., Soriano, M. C., Mirasso, C. R. & Fischer, I. Parallel photonic information processing at gigabyte per second data rates using transient states. *Nature Communications* **4**, 1364 (2013).

13. Miller, D. A. B. Attojoule Optoelectronics for Low-Energy Information Processing and Communications. *Journal of Lightwave Technology* **35**, 346–396 (2017).
14. Hamerly, R., Bernstein, L., Sludds, A., Soljačić, M. & Englund, D. Large-Scale Optical Neural Networks Based on Photoelectric Multiplication. *Physical Review X* **9**, 021032 (2019).
15. Ying, Z. *et al.* Electronic-photonic arithmetic logic unit for high-speed computing. *Nature Communications* **11**, 2154 (2020).
16. Xu, X. *et al.* 11 TOPS photonic convolutional accelerator for optical neural networks. *Nature* **589**, 44–51 (2021).
17. Feldmann, J. *et al.* Parallel convolutional processing using an integrated photonic tensor core. *Nature* **589**, 52–58 (2021).
18. Wang, T. *et al.* An optical neural network using less than 1 photon per multiplication. *arXiv preprint arXiv:2104.13467* (2021).
19. Wright, L. G. *et al.* Deep physical neural networks enabled by a backpropagation algorithm for arbitrary physical systems. *arXiv preprint arXiv:2104.13386* (2021).
20. Shen, Y. *et al.* Deep learning with coherent nanophotonic circuits. *Nature Photonics* **11**, 441–446 (2017).
21. Ríos, C. *et al.* In-memory computing on a photonic platform. *Science Advance* **5**, eaau5759 (2019).
22. Feldmann, J., Youngblood, N., Wright, C. D., Bhaskaran, H. & Pernice, W. H. P. All-optical spiking neurosynaptic networks with self-learning capabilities. *Nature* **569**, 208–214 (2019).
23. Wetzstein, G. *et al.* Inference in artificial intelligence with deep optics and photonics. *Nature* **588**, 39–47 (2020).
24. Bernstein, L. *et al.* Freely scalable and reconfigurable optical hardware for deep learning. *Scientific Reports* **11**, 3144 (2021).
25. Shastri, B. J. *et al.* Photonics for artificial intelligence and neuromorphic computing. *Nature Photonics* **15**, 102–114 (2021).

26. Lin, X. *et al.* All-optical machine learning using diffractive deep neural networks. *Science* **361**, 1004–1008 (2018).
27. Zhou, T. *et al.* Large-scale neuromorphic optoelectronic computing with a reconfigurable diffractive processing unit. *Nature Photonics* **15**, 367–373 (2021).
28. Murray, A. F., Member, S. & Edwards, P. J. Enhanced MLP Performance and Fault Tolerance Resulting from Synaptic Weight Noise During Training. *IEEE Transactions on neural networks* **5**, 792–802 (1994).
29. Moon, S., Shin, K. & Jeon, D. Enhancing Reliability of Analog Neural Network Processors. *IEEE Transactions on Very Large Scale Integration (VLSI) Systems* **27**, 1455–1459 (2019).
30. Joshi, V. *et al.* Accurate deep neural network inference using computational phase-change memory. *Nature Communications* **11**, 2473 (2020).
31. Chris M. Bishop. Training with Noise is Equivalent to Tikhonov Regularization. *Neural Computation* **7**, 108–116 (1995).
32. Blundell, C., Cornebise, J., Kavukcuoglu, K., Com, W. & Deepmind, G. Weight Uncertainty in Neural Networks. in *Proceedings of the 32nd International Conference on Machine Learning (PLMR)* 1613–1622 (2015).
33. Klachko, M., Mahmoodi, M. R. & Strukov, D. Improving Noise Tolerance of Mixed-Signal Neural Networks. in *International Joint Conference on Neural Networks (IJCNN)* 1–8 (2019).
34. Rekhi, A. S. *et al.* Analog/mixed-signal hardware error modeling for deep learning inference. in *Proceedings - Design Automation Conference* 81:1-81:6 (2019).
35. Sebastian, A. *et al.* Temporal correlation detection using computational phase-change memory. *Nature Communications* **8**, 1115 (2017).
36. Boybat, I. *et al.* Neuromorphic computing with multi-memristive synapses. *Nature Communications* **9**, 2514 (2018).
37. Mengu, D. *et al.* Misalignment Resilient Diffractive Optical Networks. *Nanophotonics* **9**, 4207–4219 (2020).

38. Mengu, D., Rivenson, Y. & Ozcan, A. Scale-, shift-and rotation-invariant diffractive optical networks. *ACS photonics* **8**, 324–334 (2021).

39. Jebara, T. *Machine Learning: Discriminative and Generative*. vol. 755 (Springer US, 2004).

40. Lasserre, J. & Bishop, C. M. Generative or Discriminative? Getting the Best of Both Worlds. *Bayesian Statistics* **8**, 3–24 (2007).

41. Bengio, Y., Thibodeau-Laufer, É., Alain, G. & Yosinski, J. Deep generative stochastic networks trainable by backprop. in *31st International Conference on Machine Learning, ICML* vol. 2 1470–1485 (2014).

42. Wu, C. *et al.* Programmable phase-change metasurfaces on waveguides for multimode photonic convolutional neural network. *Nature Communications* **12**, 96 (2021).

43. Williams, C. R. S., Salevan, J. C., Li, X., Roy, R. & Murphy, T. E. Fast physical random number generator using amplified spontaneous emission. *Optics Express* **18**, 23584–23597 (2010).

44. Xiaowen Li, Adam B. Cohen, Thomas E. Murphy & Rajarshi Roy. Scalable parallel physical random number generator based on a superluminescent LED. *Optics Letters* **36**, 1020–1022 (2011).

45. Li, P. *et al.* Parallel optical random bit generator. *Optics Letters* **44**, 2446 (2019).

46. Kim, K. *et al.* Massively parallel ultrafast random bit generation with a chip-scale laser. *Science* **371**, 948–952 (2021).

47. Goodfellow, I. J. *et al.* Generative Adversarial Nets. in *Advances in Neural Information Processing Systems* (2014).

48. Salimans, T. *et al.* Improved techniques for training GANs. *arXiv preprint arXiv:1606.03498* (2016).

49. Heusel, M., Ramsauer, H., Unterthiner, T., Nessler, B. & Hochreiter, S. GANs Trained by a Two Time-Scale Update Rule Converge to a Local Nash Equilibrium. *arXiv preprint arXiv:1706.08500* (2017).

50. Martín Abadi *et al.* TensorFlow: Large-scale machine learning on heterogeneous systems, 2015. Software available from tensorflow.org.

51. Baney, D. M., Gallion, P. & Tucker, R. S. Theory and Measurement Techniques for the Noise Figure of Optical Amplifiers. *Optical Fiber Technology* **6**, 122–154 (2000).
52. Duan, G.-H. & Georgiev, E. Non-White Photodetection Noise at the Output of an Optical Amplifier: Theory and Experiment. *IEEE Journal of Quantum Electronics* **37**, 1008–1014 (2001).
53. Yao, Z. *et al.* Integrated silicon photonic microresonators: Emerging technologies. *IEEE Journal of Selected Topics in Quantum Electronics* **24**, 1–24 (2018).
54. Seok, T. J., Kwon, K., Henriksson, J., Luo, J. & Wu, M. C. Wafer-scale silicon photonic switches beyond die size limit. *Optica* **6**, 490–494 (2019).
55. Khope, A. S. P. *et al.* Multi-wavelength selective crossbar switch. *Optics Express* **27**, 5203 (2019).
56. Yudeng Lin *et al.* Demonstration of Generative Adversarial Network by Intrinsic Random Noises of Analog RRAM Device. in *IEEE International Electron Devices Meeting* 3–4 (2018).
57. Krestinskaya, O., Choubey, B. & James, A. P. Memristive GAN in Analog. *Scientific Reports* **10**, 5838 (2020).
58. Isola, P., Zhu, J. Y., Zhou, T. & Efros, A. A. Image-to-image translation with conditional adversarial networks. in *Proceedings - 30th IEEE Conference on Computer Vision and Pattern Recognition (CVPR)* 5967–5976 (2017).
59. Turhan, C. G. & Bilge, H. S. Recent trends in deep generative models: a review. in *2018 3rd International Conference on Computer Science and Engineering (UBMK)*. 574–579 (2018).

Supplementary Information for

Harnessing Optoelectronic Noises in a Photonic Generative Adversarial Network (GAN)

Changming Wu¹, Xiaoxuan Yang², Heshan Yu³, Ruoming Peng¹, Ichiro Takeuchi³, Yiran Chen² and Mo Li^{1,4}

¹*Department of Electrical and Computer Engineering, University of Washington, Seattle, WA 98195, USA*

²*Department of Electrical and Computer Engineering, Duke University, Durham, NC 27708, USA*

³*Department of Materials Science and Engineering, University of Maryland, College Park, MD 20742, USA*

⁴*Department of Physics, University of Washington, Seattle, WA 98195, USA*

I. Theory and process flow for O/E random number generator (RNG)

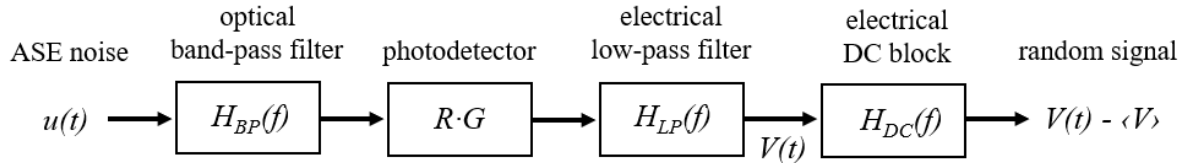


Fig. S1 The block diagram showing the key component and the process flow in the random number generation procedure using the ASE noise as the input.

In this work, we followed the same method developed by Williams et al.¹ to generate random signals from the ASE noise. Fig. S1 shows the process flow to generate random signals. The input signal $u(t)$ is the optical random noise produced from amplified spontaneous emission (ASE) and has a broadband power spectral density (PSD) $S_{in}(f)$, as shown in Fig. 2a in the main text. The input is first spectrally filtered after passing an optical band-pass filter with the frequency response $H_{BP}(f)$. Due to the narrow bandwidth of the band-pass filter H_{BP} , the PSD within the bandwidth is approximated as a constant S_{in} and the PSD after the band-pass filter becomes $S_{in}|H_{BP}(f)|^2$. The filtered optical signal is then detected by a square-law photodetector and further passes an electrical low-pass filter with the frequency response $H_{LP}(f)$ and the bandwidth B_{LP} , generating noisy baseband electrical voltage signals from the beating between different optical frequency

components, which are referred to as “ASE-ASE beat noises”. In practice, the photodetector plays the role of both the power meter and the low-pass filter. Here, we assume the power responsivity and the gain of the photodetector are constants, R (in V/mW) and G , respectively. The frequency responses of the band-pass and low-pass filters are Gaussian following:

$$|H_{BP}(f)|^2 = \exp \left[-(4 \ln 2) \frac{(f - f_0)^2}{B_{BP}^2} \right], \quad |H_{LP}(f)|^2 = \exp \left[-(\ln 2) \frac{f^2}{B_{LP}^2} \right].$$

where f_0 is the center frequency of the band-pass filter. As a result, PSD of the voltage noise S_{noise} obtained after the electrical DC block is given by the multiplication between total integration of optical noise power and the photodetector gain and responsitivity, is a Gaussian:

$$\begin{aligned} S_{noise}(f) &= R^2 G^2 S_{in}^2 |H_{LP}(f)|^2 \int |H_{BP}(f') H_{BP}(f' + f)|^2 df' \\ &= R^2 G^2 S_{in}^2 B_{BP} \sqrt{\frac{\pi}{8 \ln 2}} \exp \left[-(\ln 2) \left(\frac{1}{B_{LP}^2} + \frac{2}{B_{BP}^2} \right) f^2 \right]. \end{aligned}$$

The corresponding voltage variance at the final output thus is given by:

$$\begin{aligned} \sigma_{noise}^2 &= \int S_{noise}(f) df = R^2 G^2 S_{in}^2 \int \int |H_{LP}(f) H_{BP}(f') H_{BP}(f' + f)|^2 df' df \\ &= R^2 G^2 S_{in}^2 B_{BP} \sqrt{\frac{\pi}{4 \ln 2}} (1 + \frac{B_{BP}^2}{2 B_{LP}^2})^{-1/2}. \end{aligned}$$

In practice, we control the mean power of the ASE noise (DC component), $S_{in} H_{LP}(0) \int |H_{BP}(f)|^2 df = S_{in} B_{BP} \sqrt{\frac{\pi}{4 \ln 2}}$, and make sure that it will not saturate the photodetector.

II. Measurement setup for photonic convolutional tensor core

The experimental setup used to carry out the convolution operations with a 2×2 matrix (see Fig. 1 of the main text) is shown in Fig. S2. We follow the same process of operating the photonic network as described in Wu *et.al*². The input vector is encoded as the temporal modulated optical signal from four different wavelength channels. Another laser connected to a 1×4 optical switch is

used to selectively set the mode contrast of individual PMMC, which represents a single kernel weight element. The MVM operation is reduced to the mode contrast measurement. The resulting transmitted power of TE_0 and TE_1 modes are summed incoherently using photodetectors. Their difference is calculated electronically and used in post-processing steps. The TE_0 mode output coming from all the PMMCs is combined using on-chip Y-junctions, while the TE_1 mode output power is combined off-chip because the same ports are used to program the PMMCs optically. Because combining four incoherent sources using Y-junctions will inherently reduce the power by a factor of 4, we rescaled the measured TE_0 mode power by this factor when calculating the power differences between the two modes.

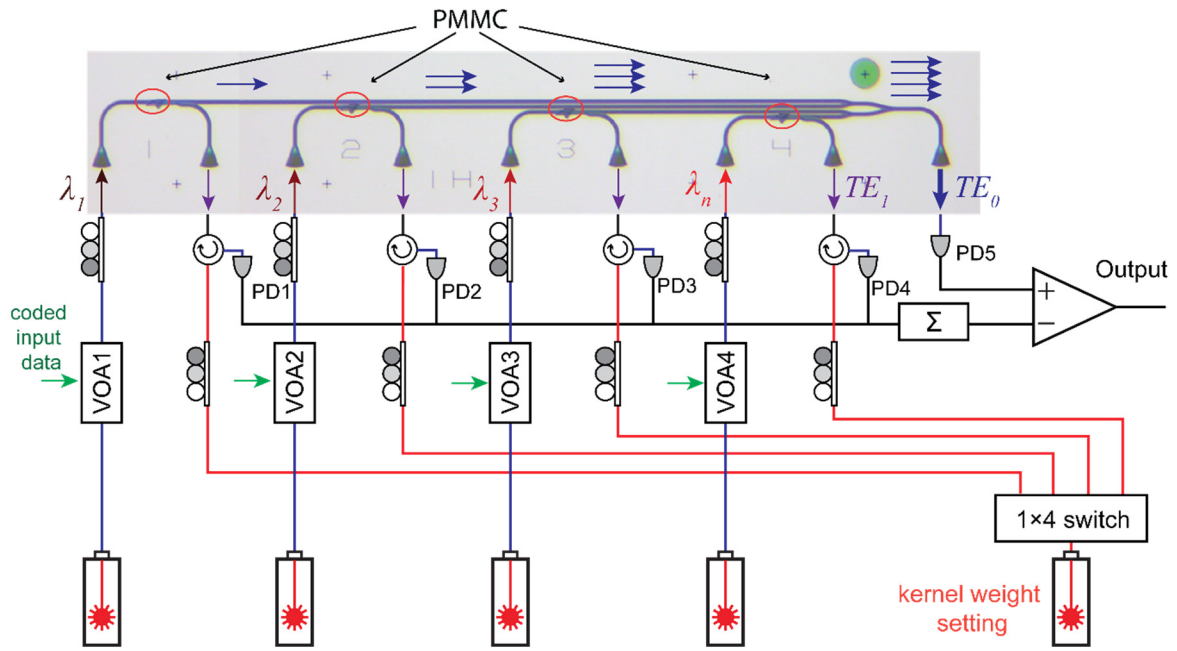


Fig. S2 Experimental setup for convolutional MVM operation. The input vector is encoded as the temporal modulated optical signal from four different wavelength channels and sent into four PMMCs (solid blue lines). Another laser connected to a 1×4 optical switch is used to selectively set the mode contrast of individual PMMC, which represents a single kernel weight element (solid red lines). The MVM operation is reduced to the mode contrast measurement. The total TE_0 mode power is collected on-chip using Y junctions while the TE_1 mode power is collected off-chip by an external electrical circuit (solid black lines).

III. MVM error analysis for PMMC based photonic tensor core

The key to generating high quality handwritten number images is to perform accurate matrix-vector multiplication (MVM) operations, $\mathbf{Y}^l = \mathbf{W}^l \cdot \mathbf{X}^l$, where \mathbf{Y}^l is the output matrix, \mathbf{W}^l is the kernel

matrix and \mathbf{X}^l is the input vector of the layer l . In practice the noise is inevitably introduced through non-ideal pieces of equipment, leading to errors on both input vector \mathbf{X}^l and the kernel matrix \mathbf{W}^l , the realistic MVM operation will give the results $\mathbf{Y}' = \mathbf{Y}^l + \Delta \mathbf{Y}^l = (\mathbf{W}^l + \Delta \mathbf{W}^l) \cdot (\mathbf{X}^l + \Delta \mathbf{X}^l) \approx \mathbf{W}^l \cdot \mathbf{X}^l + \Delta \mathbf{W}^l \cdot \mathbf{X}^l + \mathbf{W}^l \cdot \Delta \mathbf{X}^l$, where $\Delta \mathbf{Y}^l$, $\Delta \mathbf{W}^l$, $\Delta \mathbf{X}^l$ are the errors for the corresponding elements. $\Delta \mathbf{X}^l$ is mainly caused by the inaccurate response of the EOM at the input. $\Delta \mathbf{W}^l$ is caused by mode contrast setting error, $\Delta \Gamma^l$, which includes short-term mode contrast setting inaccuracy $\delta \Gamma$ (write noise) as well as the long-term measurement fluctuations (read noise) such as the drift of the measurement setup over time. The ratio between the two error terms contribute to the element Y_i^l of layer l during the MVM calculation is estimated by:

$$\frac{(\Delta \mathbf{W}^l \cdot \mathbf{X}^l)_i}{(\mathbf{W}^l \cdot \Delta \mathbf{X}^l)_i} = \frac{\sum \Delta w^l_{ij} x^l_j}{\sum w^l_{ij} \Delta x^l_j} \approx \frac{\langle \frac{|\Delta w^l|}{|w^l|} \rangle}{\langle \frac{|\Delta x^l|}{|x^l|} \rangle} \approx \frac{\frac{\Delta \Gamma^l}{\langle |\Gamma^l| \rangle}}{\frac{\delta |x^l|}{\langle |x^l| \rangle}},$$

where the $\Delta \Gamma^l$ and $\delta |x^l|$ are the standard deviations (STD) of mode contrast setting error and the input error, $\langle |\Gamma^l| \rangle$ and $\langle |x^l| \rangle$ are the mean values of the mode contrast setting error and the input error. Take the first layer as an example, the $\langle x^l \rangle$ and $\delta |x^l|$ are 0.1723 and 8×10^{-4} respectively (see Fig.S3). The $\langle |\Gamma^l| \rangle$ and $\Delta \Gamma^l$ are 0.4236 and 0.05 for weight setting error (0.007 for short-term write noise $\delta \Gamma$). The ratio between the two error terms is 25.42 (4.07 only short-term write noise considered), thus the input setting error will not be the main noise source in our photonic GAN.

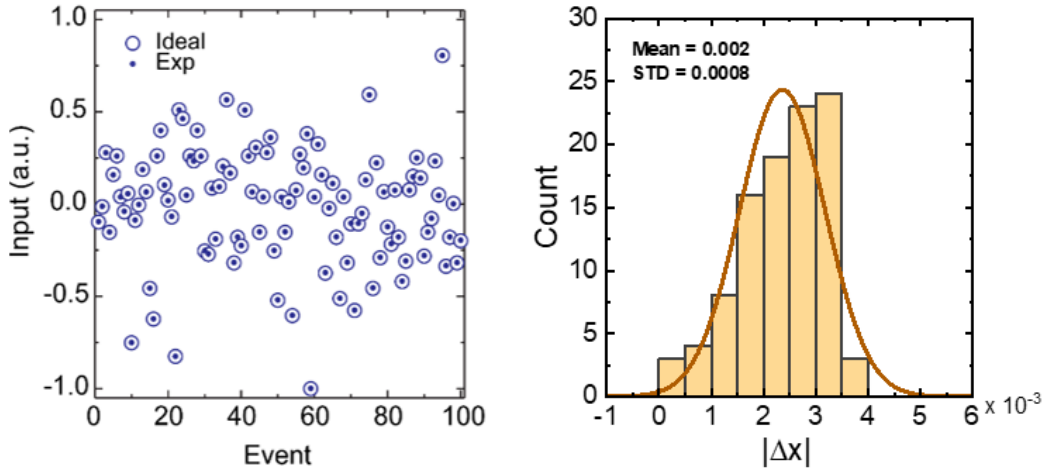


Fig. S3 a. An encoded optical signal trace is used as the input in the first layer obtained from measurement with its corresponding ideal value. **b.** The histogram of the input signal error is defined as $|\Delta x| = |x_{\text{experiment}} - x_{\text{ideal}}|$. The standard deviation is only 8×10^{-4} , much smaller than the STD of short-time mode contrast setting error $\delta \Gamma$ ($\sim 0.8\%$) and the overall contrast setting error $\Delta \Gamma^l$ ($\sim 5\%$).

IV. Noise-Aware training Method for GAN network

Fig. S4 shows the three noise-aware training approaches we proposed in the main text, the IC-GAN, the WC-GAN and the CR-GAN respectively. All three approaches are based on the off-line training configuration that we first train the GAN on a digital computer. After the network is trained, we mapped the obtained parameters to the photonic hardware for further implementation.

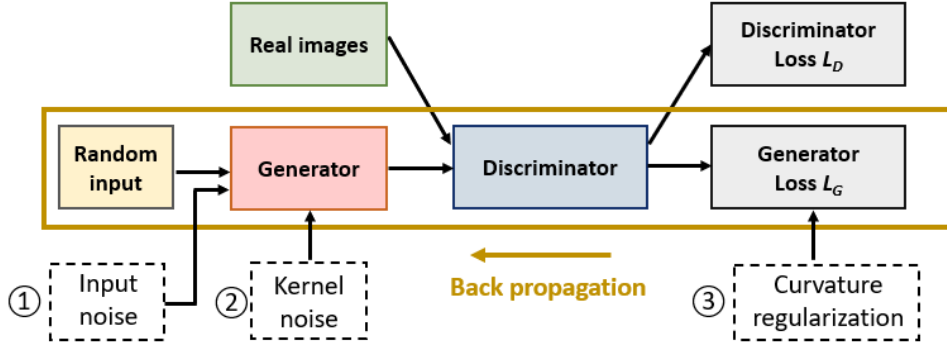


Fig. S4 Schematic of the noise-aware training approaches for the generator in GAN. The parameters in the discriminator are held constant while the parameters in the generator are updated through the backward-propagation process. In the forward propagation process, the noise is added on the (1) random input (for IC-GAN) or (2) the kernel weights (for WC-GAN) to enhance the stability of the GAN against the practical noise. An alternative approach is to (3) introduce the curvature regularization term in the loss function (CR-GAN) to avoid dropping into a local minimum that is sensitive to weight variation.

The IC-GAN approach inflates the STD of the random signal input, 0.5 in our case, during training of the network, while all the other steps in the forward and backward-propagation pass such as the loss function calculation, the gradient descent and weight update, are the same as the conventional GAN training algorithm. We control the learning rates for the discriminator and the generator are the same value, 1×10^{-4} , to avoid one overpowering the other. Once all the parameters are obtained, we implement the network in practice only use noise with a smaller STD (0.2 in our experiment) as the input.

For the WC-GAN approach, we cast the effect of all the error sources into the single 5% STD Gaussian noise ΔW_{ij} and add the noise onto the corresponding kernel weight at each forward-propagation pass. As shown in Fig. S5a, the introduced noise on kernel weight gives a deviation of the loss function L'_G from its ideal value L_G thus leads to a different gradient. The WC-GAN

performs noiseless gradient descent and weight update in the back-propagation pass based on the L'_G . According to the mapping condition, $\Delta W_{ij}^l = \frac{|W|_{max}^l}{|\Gamma|_{max}^l} \cdot \Delta \Gamma_{ij}^l$, the total noise injected ΔW_{ij}^l on corresponding kernel weight during training is closely related to the maximum weight absolute value, thus the noise may grow uncontrollably with growing maximum weight values and prevent the training to converge. Therefore we clip the kernel weight distribution in the desired range by rescaling the kernel element with the maximum absolute value of each layer by a factor (of 0.995 in the training) after every weight update. The weight clipping process improves the GAN training convergence. All the other steps in the WC-GAN training approach are the same as the conventional algorithm.

For the CR-GAN approach (see Fig. S4b), we assume the robustness to practical noise of the model can be maximized if the distance between the weight gradient at the point \mathbf{W}^l in parametric hyperspace and the gradient of neighborhood points \mathbf{W}'^l are minimized. We define the regularization term L_r as the maximal distance between the weight gradient and the gradient of neighborhood point $L_r = \left\| \frac{dL_G}{d\mathbf{W}^l} - \frac{dL'_G}{d\mathbf{W}'^l} \right\|$ where the range of neighborhood is defined by the discretization step h . In each training step, the regularization term is added to the total loss $L_{wr} = L_G + rL_r$ where r is the regularization strength and then the back-propagation is performed on the weights. In our simulation, the h and r vary under various noise levels to obtain optimal performance.

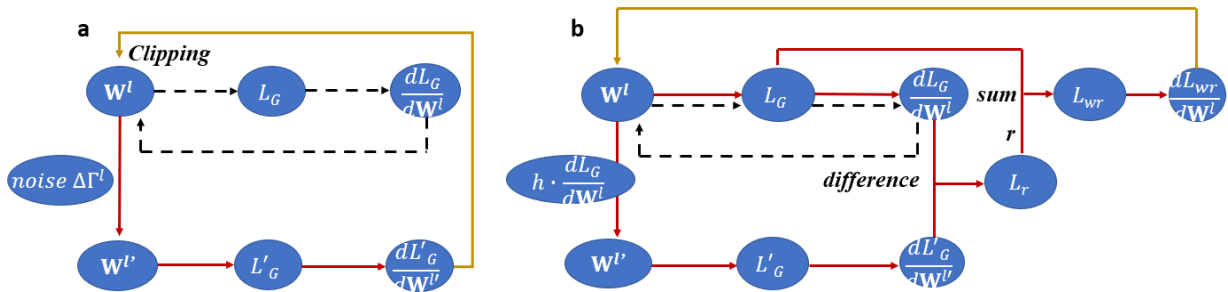


Fig. S5 Schematic of the kernel weight update process for **(a)** WC-GAN and **(b)** CR-GAN respectively. The solid red line and the solid yellow line indicate the forward-propagation pass and the backward-propagation pass respectively. The dashed black line indicates the conventional GAN training process.

V. The architecture of the GAN to generate the handwritten number

We use two GAN networks to generate the handwritten number “7” and the full 10 digits from “0” to “9” respectively.

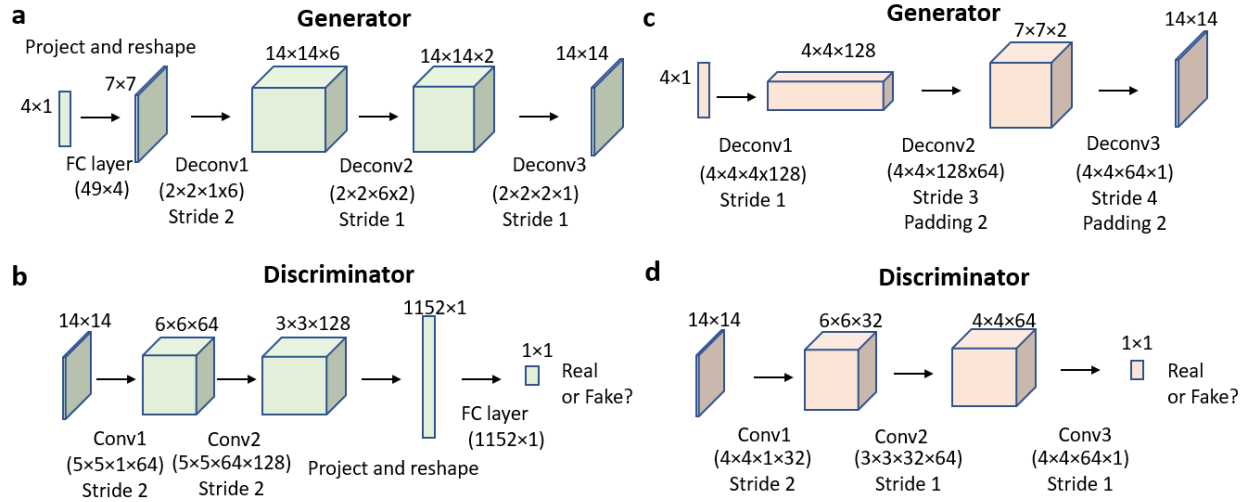


Fig. S6 a and b: the architecture of the (a) generator and (b) discriminator in original GAN, WC-GAN and IC-GAN that are used to generate handwritten number “7”. **c and d:** the architecture of the (c) generator and (d) discriminator in original GAN and CR-GAN that are used to generate the full handwritten digits from “0” to “9”.

The generator models in the GAN (see Fig. S6a and S6c) are composed of the fully connected layer (FC) and deconvolution layers (Deconv). After each hidden layer, batch normalization is operated before applying the nonlinear function. For the generator to generate “7” (Fig. S6a), we choose the LeakyReLu as the nonlinear function after each hidden layer and for the generator to generate full digits (Fig. S6c), we choose the ReLu as the nonlinear function. For both models, we use the hyperbolic tangent function as the nonlinear function at the final output.

The discriminators in the GAN (see Fig. S6b and S6d) are composed of the FC layer (FC) and convolution layers (Conv). For both discriminator models, we choose the LeakyReLu as the nonlinear function after each hidden layer and apply the sigmoid function at the final output.

VI. The hand-written numbers generated using accurate kernel and inaccurate kernel matrices.

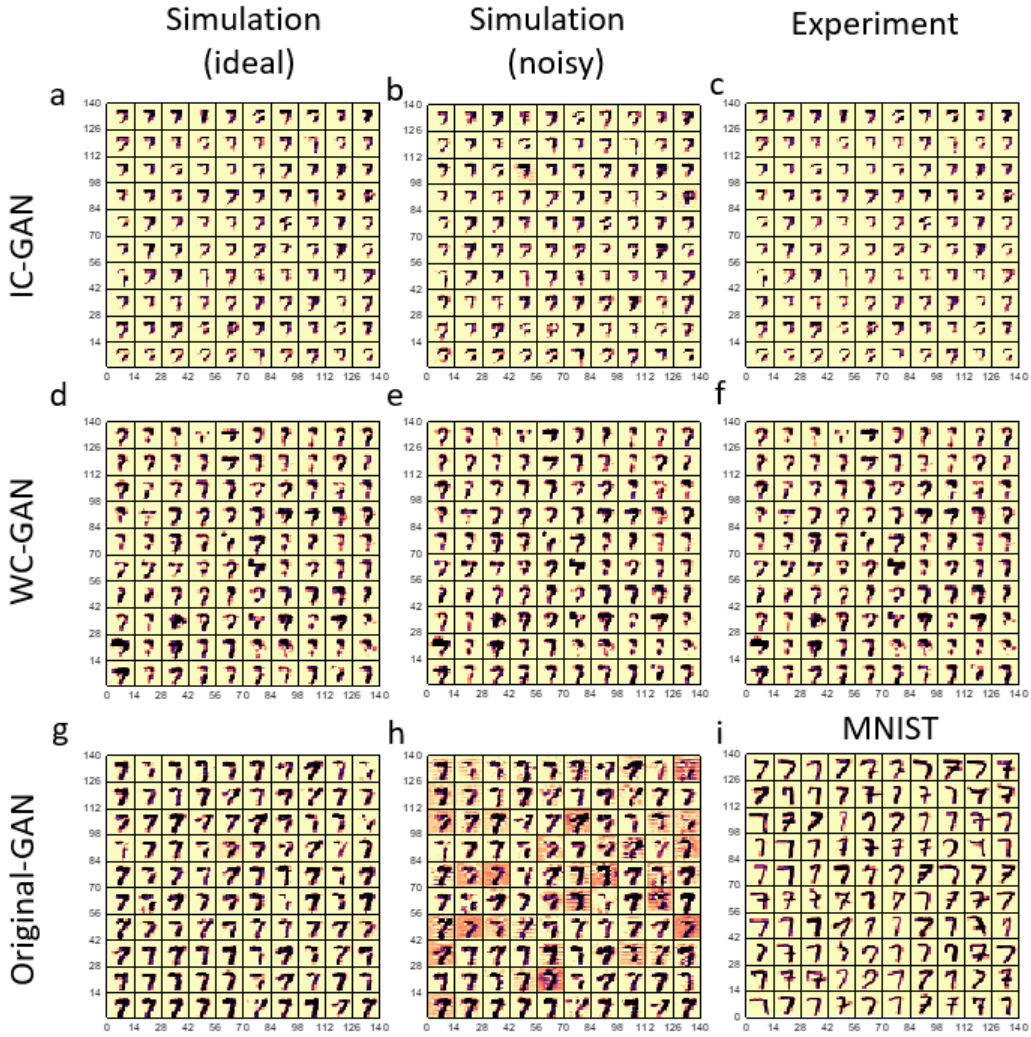


Fig. S7 Images of the handwritten number “7” generated by (a-c) the IC-GAN, (d-f) the WC-GAN and (g-h) the original GAN using the (i) MNIST as the training database. The results show that the IC-GAN and WC-GAN are less vulnerable to practical noise.

Fig. S7 shows the images of the handwritten number “7” generated by the IC-GAN (see Fig. S7a-S7c), the WC-GAN (see Fig. S7d-S7f) and the original GAN (Fig S7g, S7h) respectively using the (i) MNIST dataset as the training database. The simulation results assuming the noisy kernel weights (Fig. S7b and S7e) are consistent with our experimental results (Fig. S7c and S7f). The results also show that compared to the original GAN, the IC-GAN and WC-GAN are less vulnerable to practical noise. The images of the full 10 digits from “0” to “9” generated by the

original GAN and the CR-GAN under the mode contrast setting error ranging from 0% to 10% are shown in Fig. S8 and Fig. S9.

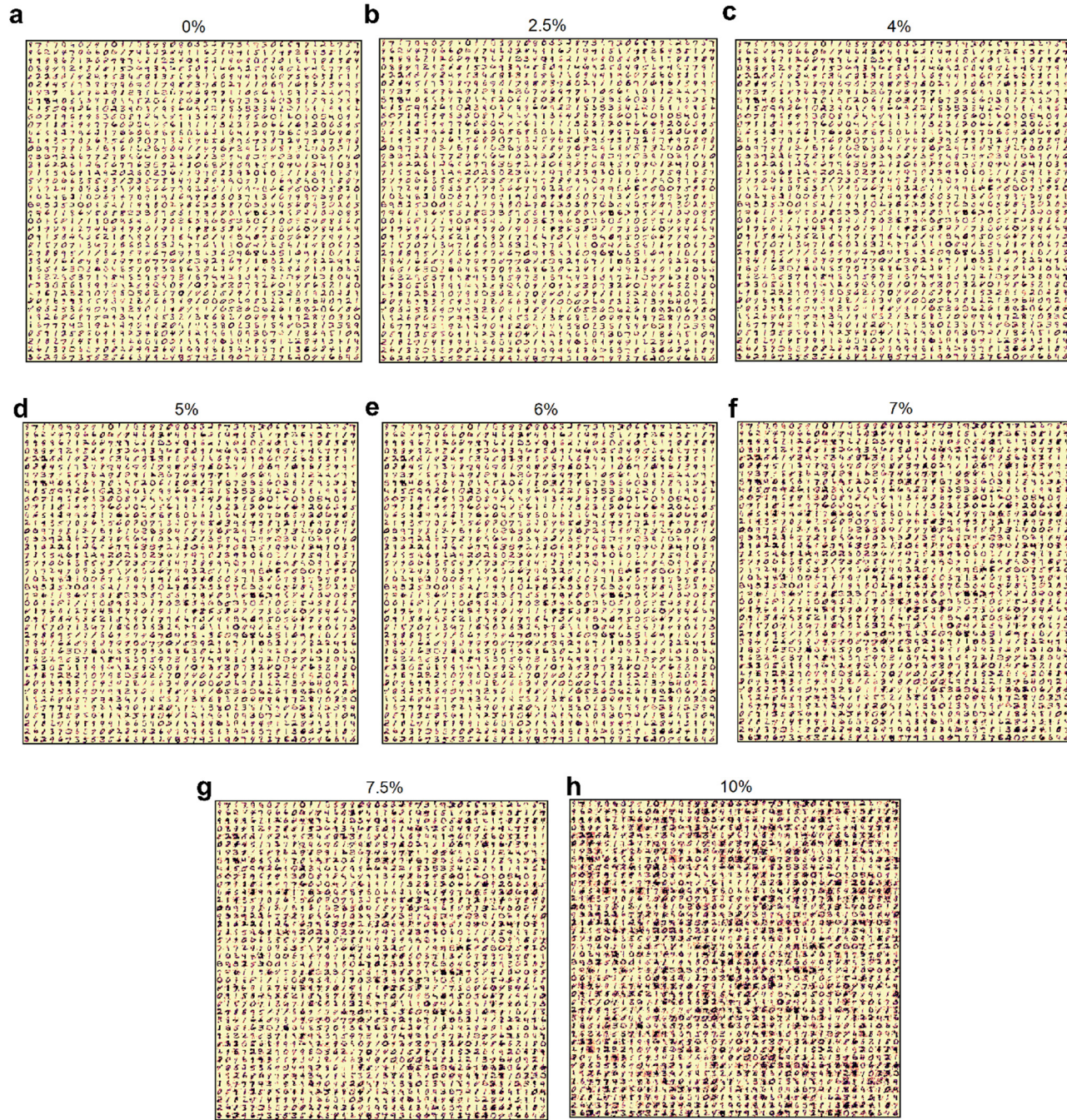


Fig. S8 The images of the full 10 digits from “0” to “9” generated by the CR-GAN in simulation assuming the mode contrast setting error is (a) 0% (ideal), (b) 2.5%, (c) 4%, (d) 5%, (e) 6%, (f) 7% (g) 7.5% and (h) 10%, respectively.

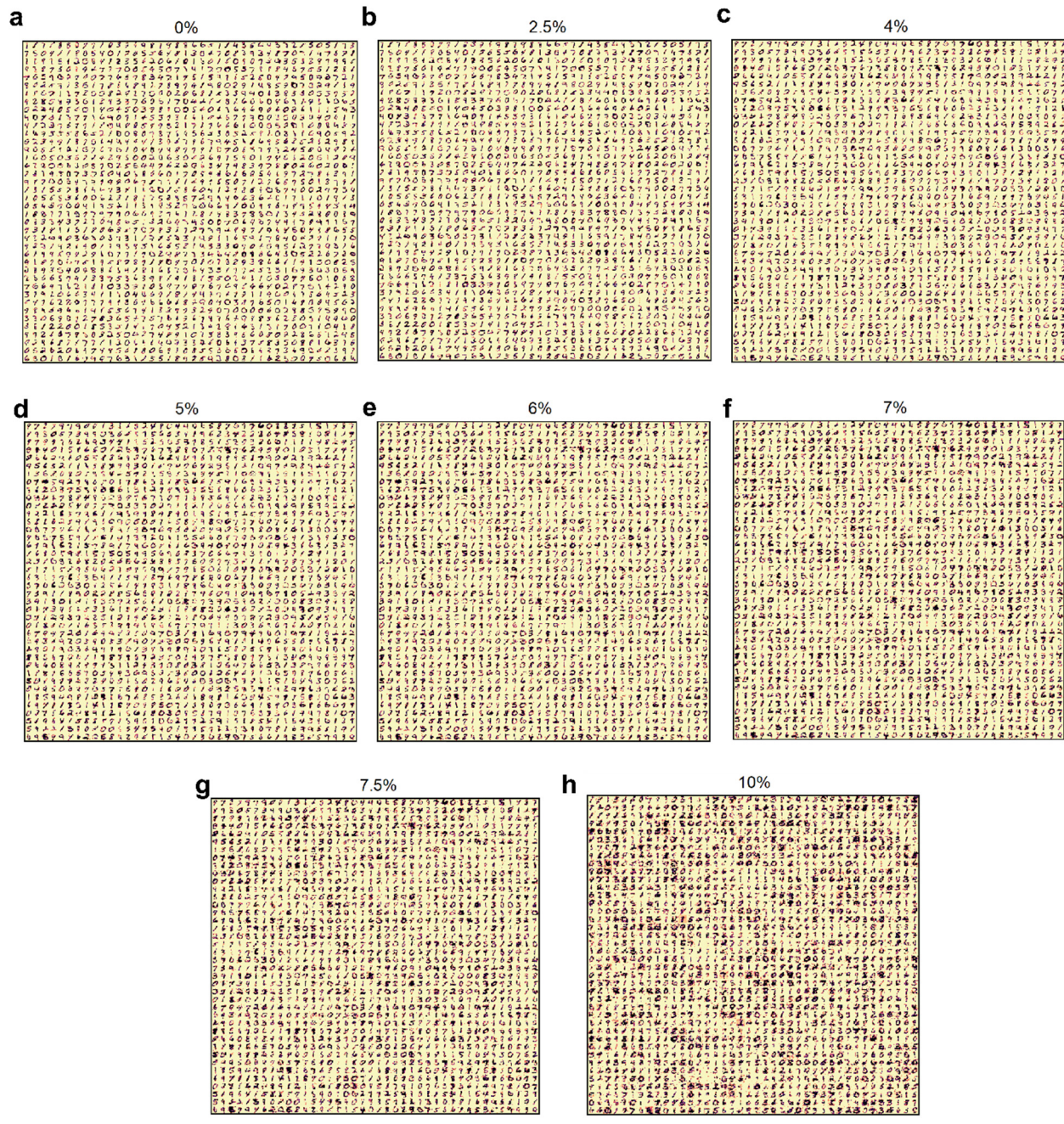


Fig. S9 The images of the full 10 digits from “0” to “9” generated by the CR-GAN in simulation assuming the mode contrast setting error is (a) 0% (ideal), (b) 2.5%, (c) 4%, (d) 5%, (e) 6%, (f) 7% (g) 7.5% and (h) 10%, respectively.

VII. Calculate FID and estimate the diversity of the generated images

The Frechet inception distance (FID) is a metric for evaluating the quality of generated images from both fidelity and diversity and is proposed to specifically evaluate the performance of generative adversarial networks by Martin Heusel et al. in 2017³. To calculate FID, we design another CNN as shown in Fig. S10 to classify the generated handwritten digits. The overall error rate of this CNN is only 2.43% after training. When a 14×14 image is sent into this network, the activation features obtained before the last fully connected layer is reshaped as the “feature vector” with the size 160×1 and the n feature vectors obtained after n images fed into the CNN are further combining together to form a feature matrix with the size of $160 \times n$. The FID evaluates generated images by statistically comparing the generated images with the real images from the target domain. Assuming the matrices \mathbf{X} and \mathbf{Y} are the feature matrices for the GAN generated images and the real images from MNIST database respectively, the FID then is defined as:

$$FID = \|\mu_X - \mu_Y\|^2 + \text{tr} \left(\Sigma_X + \Sigma_Y - 2(\Sigma_X \Sigma_Y)^{\frac{1}{2}} \right),$$

where μ_X and μ_Y refer to the feature-wise mean vectors of the GAN-generated images and real images, Σ_X and Σ_Y are the covariance matrices of the corresponding feature matrix \mathbf{X} and \mathbf{Y} , and “ tr ” refers to the trace operation. To perform more accurate FID results in this work, we also break the generated images into groups and calculate the mean and standard deviation of the FID.

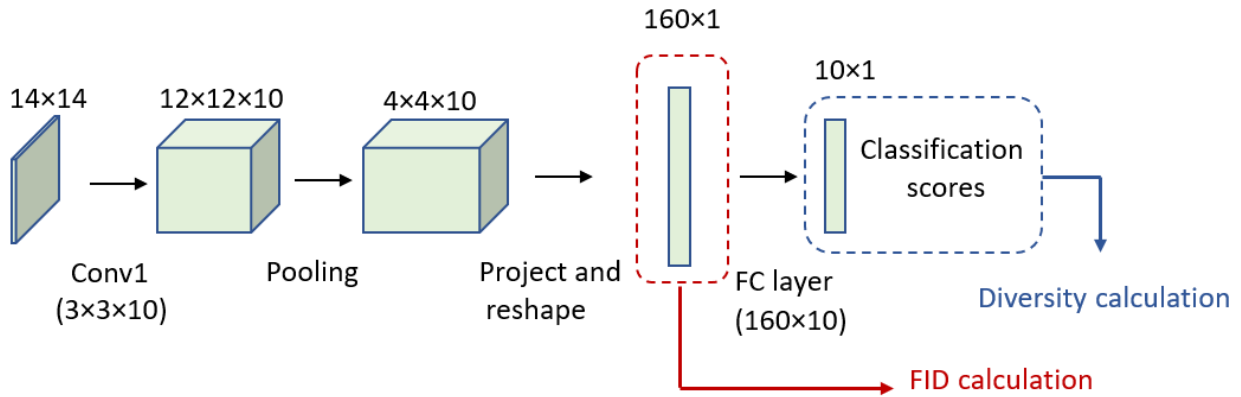


Fig. S10 The architecture of the convolutional neural network is used for handwritten digits classification. When a 14×14 image is sent into this network, the activation features obtained before the last fully connected layer is reshaped as the “feature vector” with the size 160×1 to calculate the FID. The statistics of the classification results are used to estimate the diversity.

We also estimate the diversity of generated images using the diversity coefficient, which is defined as the STD of the percentage of each number classes in the generated images:

$$\text{Diversity Coefficient} = \sqrt{\frac{\sum_{i=0}^9 \left| P_i - \frac{1}{10} \right|^2}{10}}$$

Where P_i is the statistic percentage for the generated image is successfully classified as the number “ i ”, i is the digit number from 0 to 9. The more diversity the generated images have, the more uniform the percent of ten classes and the lower the diversity coefficient is. For example, for the MNIST training database which has a close-to-uniform percent of ten classes, the diversity coefficient is as low as 0.00585 (see the solid black horizontal line in Fig. S11). Fig. S11 shows the diversity coefficient of images generated by the original GAN and the CR-GAN as a function of the mode contrast error. As the noise level increases from 0% (ideal) to 8%, the diversity coefficient gradually drops, which supports our claim in the main text that the diversity of the generated images increases with a larger noise. The increase of the diversity coefficient at 10% mode contrast setting error is due to the breakdown of the classification accuracy of the CNN, the quality of the generated images is so bad that CNN can not give the correct class of the generated image.

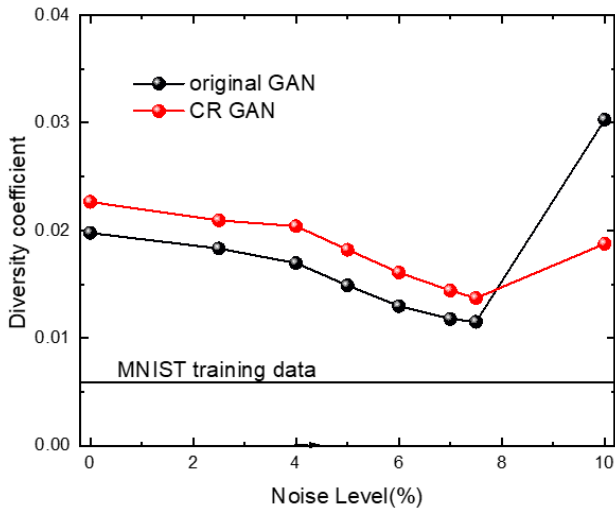


Fig. S11 The diversity coefficient of the generated images by original GAN and CR-GAN respectively under various effective noise ΔI_{ij}^l with STD ranging from 0% to 10%.

Reference:

1. Williams, C. R. S., Salevan, J. C., Li, X., Roy, R. & Murphy, T. E. Fast physical random number generator using amplified spontaneous emission. *Optics Express* **18**, 23584–23597 (2010).
2. Wu, C. *et al.* Programmable phase-change metasurfaces on waveguides for multimode photonic convolutional neural network. *Nature Communications* **12**, 96 (2021).
3. Heusel, M., Ramsauer, H., Unterthiner, T., Nessler, B. & Hochreiter, S. GANs Trained by a Two Time-Scale Update Rule Converge to a Local Nash Equilibrium. *arXiv preprint arXiv:1706.08500* (2017).
4. Yudeng Lin *et al.* Demonstration of Generative Adversarial Network by Intrinsic Random Noises of Analog RRAM Device. in *IEEE International Electron Devices Meeting (IEDM)* 3–4 (2018).